



# Direct validation of dune instability theory

Ping Lü<sup>a,1,2</sup>, Clément Narteau<sup>b,1,2</sup>, Zhibao Dong<sup>a</sup>, Philippe Claudin<sup>c</sup>, Sébastien Rodriguez<sup>b</sup>, Zhishan An<sup>d</sup>, Laura Fernandez-Cascales<sup>b</sup>, Cyril Gadal<sup>b</sup>, and Sylvain Courrech du Pont<sup>e</sup>

<sup>a</sup>School of Geography and Tourism, Shaanxi Normal University, Xi'an, Shaanxi 710119, China; <sup>b</sup>Université de Paris, Institut de physique du Globe de Paris, CNRS, F-75005 Paris, France; <sup>c</sup>Physique et Mécanique des Milieux Hétérogènes, CNRS, Ecole Supérieure de Physique et de Chimie Industrielles de la Ville de Paris, Paris Science & Lettres Research University, Sorbonne Université, Université de Paris, 75005 Paris, France; <sup>d</sup>Northwest Institute of Eco-Environment and Resources, Lanzhou, Gansu Province 730000, China; and <sup>e</sup>Laboratoire Matière et Système Complexes, Université de Paris, CNRS, 75205 Paris Cedex 13, France

Edited by Harry L. Swinney, University of Texas at Austin, Austin, TX, and approved March 26, 2021 (received for review November 20, 2020)

**Modern dune fields are valuable sources of information for the large-scale analysis of terrestrial and planetary environments and atmospheres, but their study relies on understanding the small-scale dynamics that constantly generate new dunes and reshape older ones. Here, we designed a landscape-scale experiment at the edge of the Gobi desert, China, to quantify the development of incipient dunes under the natural action of winds. High-resolution topographic data documenting 42 mo of bedform dynamics are examined to provide a spectral analysis of dune pattern formation. We identified two successive phases in the process of dune growth, from the initial flat sand bed to a meter-high periodic pattern. We focus on the initial phase, when the linear regime of dune instability applies, and measure the growth rate of dunes of different wavelengths. We identify the existence of a maximum growth rate, which readily explains the mechanism by which dunes select their size, leading to the prevalence of a 15-m wavelength pattern. We quantitatively compare our experimental results with the prediction of the dune instability theory using transport and flow parameters independently measured in the field. The remarkable agreement between theory and observations demonstrates that the linear regime of dune growth is permanently expressed on low-amplitude bed topography, before larger regular patterns and slip faces eventually emerge. Our experiment underpins existing theoretical models for the early development of eolian dunes, which can now be used to provide reliable insights into atmospheric and surface processes on Earth and other planetary bodies.**

to the topography and a stabilizing process due to transport inertia (20).

Fluid mechanics studies have shown that the flow above low dunes can be decomposed into an inner layer and an outer layer (21). In the outer layer, the flow perturbation is in phase with topography (i.e., wind speed is maximum above the dune crest). In the inner layer (the thin region adjacent to the bed), the effect of friction causes the wind velocity to be phase advanced (22, 23). The theory predicts that this layer has a thickness,  $l$ , that shows a positive dependence on the wavelength,  $\lambda$ , of the bedforms. Within this layer, the maximum (minimum) wind speed is upwind of the maximum (minimum) of topography. For a sinusoidal topography, this perturbation takes the form of a phase shift,  $\varphi_b$ , which is usually described with two terms,  $\cos(kx + \varphi_b) = A \cos(kx) + B \cos(kx + \pi/2)$ , where  $k = 2\pi/\lambda$  is the dune wave number. The in-phase term has a weight coefficient  $A$ . The other, in phase quadrature, has a weight coefficient  $B$ . Then, the upwind shift between the wind speed and the bed topography can be expressed as  $\arctan(B/A)/k$ . Since the dune crest is a zone of decreasing wind speed and therefore, of sand deposition, this spatial shift is the essential ingredient for the initial growth of dunes (24). Nevertheless, the length scale associated with this spatial shift does not alone promote the dominance of any specific wavelength. Wavelength selection requires another antagonistic process, which relies on sand transport properties.

As sand flux adjusts to the aforementioned spatial change in wind speed, there is a spatial lag between the loci of maximum

dune | instability | size selection | sediment transport | surface winds

**D**une research has always been stimulated by the question of the origin of periodic bedforms that are ubiquitous in sand seas at all scales (1–3). Answering this question has proven challenging, largely because of the variety of initial and boundary conditions spanned by places where regular dune patterns are observed (4–6). In addition, considerable uncertainty exists on the efficiency of the mechanisms of dune size selection due to a dearth of reliable experiments on eolian dune growth. Quantitative analysis of incipient dune formation is therefore a prerequisite for a better physical understanding not only of the evolution of dune systems but also, of transport and flow properties responsible for the emergence of a characteristic length scale.

Underwater experiments have shown that, as soon as the flow is strong enough to transport grains, a flat sand bed destabilizes into periodic bedforms propagating at a constant speed (7–14). However, wind tunnel experiments and Ralph Bag-nold's attempts in the field to create artificial dunes have failed because the initial sand piles were not large enough (15, 16). There is indeed a minimum length scale for the formation of dunes, which has been estimated to be of the order of 10 m in eolian systems on Earth based on the smallest wavelength of the superimposed bedforms observed on the flanks of large dunes (17–19). After 20 y of intensive research, this characteristic length scale is assumed to be regulated by the balance between a destabilizing process associated with the turbulent flow response

## Significance

**We report a landscape-scale experiment with controlled initial and boundary conditions to reveal incipient dune growth under natural action of wind. We measured growth rate of dunes of different wavelengths for 42 mo in a desert plot of 7,500 m<sup>2</sup>. We identify an early phase in which a clear maximum growth rate occurs for a 15-m dune spacing. Successful comparison with dune instability theory allows us to quantify the size-selection mechanism leading to the emergence of periodic dune patterns, which can be directly related to flow and sand transport properties. An experiment of this type and scale is unprecedented. Its results boost confidence in the existing theory, confirming its application to a variety of planetary landscapes from repeated aerial/orbital imagery.**

Author contributions: P.L., C.N., Z.D., P.C., S.R., and S.C.d.P. designed research; P.L., C.N., P.C., S.R., Z.A., L.F.-C., and S.C.d.P. performed research; P.L., C.N., and C.G. analyzed data; and P.L., C.N., P.C., S.R., and S.C.d.P. wrote the paper.

The authors declare no competing interest.

This article is a PNAS Direct Submission.

Published under the [PNAS license](#).

<sup>1</sup>P.L. and C.N. contributed equally to this work.

<sup>2</sup>To whom correspondence may be addressed. Email: lvping@snnu.edu.cn or narteau@ippg.fr.

This article contains supporting information online at <https://www.pnas.org/lookup/suppl/doi:10.1073/pnas.2024105118/-/DCSupplemental>.

Published April 21, 2021.

wind speed and maximum transport rate (25–27). This length scale is known as the saturation length  $l_{\text{sat}}$ , the distance required for the sand flux to reach saturation. The combined effect of this downwind shift in sand transport and the upwind shift in wind speed eventually acts as a size-selection mechanism. The minimum length scale for the formation of dunes arises at a characteristic wave number,  $k_0$ , defined as the wave number for which these downwind and upwind shifts cancel each other out. At longer wavelengths ( $k < k_0$ ), the crest is a zone of net deposition such that the dune grows. However, larger bedforms have longer response times, which means that the growth rate also tends to 0 in the limit  $k \rightarrow 0$ . There is therefore a characteristic wave number,  $k_{\text{max}}$ , for which the growth rate is maximum. It determines the most unstable wavelength,  $\lambda_{\text{max}}$ , and the characteristic length scale for the emergence of periodic dunes.

Linear stability analysis of flat sand beds sheared by a fluid flow provides the analytical expression for the growth rates  $\sigma(k)$  of sinusoidal bed perturbations over the whole range of possible wavelengths (6–8, 14, 16, 28). These stability analyses are by definition restricted to the linear regime of incipient dune growth, the period during which the amplitude of each mode (wavelength) grows exponentially and independently from one another. In this linear regime, a dispersion relation gives the growth rate of each mode as a function of the wave number. According to the flow and transport processes described above, theoretical dispersion relation can be expressed as

$$\sigma(k) = Q k^2 \frac{B - A k l_{\text{sat}}}{1 + (k l_{\text{sat}})^2}, \quad [1]$$

where  $Q$  is the mean sand flux, which can be derived from wind data and the threshold shear velocity,  $u_{\text{th}}$ , for the transport of sand grains (20). The numerator not only governs the initial dune growth [i.e.,  $\sigma(k) > 0$  for  $k < k_0$  and  $\sigma(k) < 0$  for  $k > k_0$ , where  $k_0 = B/(A l_{\text{sat}})$ ] but also, provides the essential mechanism for dune size selection during the linear regime. Later, as dune aspect ratios become larger, dune dynamics enter a non-linear growth regime dominated by collisions and interactions between dunes of different sizes (35–39), and this dispersion relation no longer applies.

Focusing only on well-established periodic dune patterns, the existence of a characteristic wavelength for dune formation has been validated in various eolian environments using tools of comparative planetology (29) and in different places on Earth

using superimposed bedforms (17) as well as incipient dunes in ephemeral channels (40) or at the border of dune fields (5). However, the dependence of the growth rate on dune size and the underlying size-selection mechanism associated with the emergence of periodic dunes have never been observed and quantified in a natural eolian environment, nor in wind tunnels. To bridge this gap, we performed a long-term field experiment to measure, in the same desertic area, all of the parameters involved in the physics of dune growth. We present here a comprehensive description of incipient dune growth under the natural action of wind, which is directly confronted to the dune instability theory.

## A Landscape-Scale Experiment

In our landscape-scale experiments, we investigated dune dynamics at a scale of hundreds of meters using controlled initial conditions and continuous monitoring of environmental conditions (41). These experiments started in 2009 in the Tengger desert at the southeastern edge of the Gobi basin in China (Fig. 1A). This area is exposed to a bidirectional wind regime (Fig. 1B). The primary wind blows from the northwest mainly in the spring when the Siberian high-pressure system weakens. In summer, the easterly wind of the east Asian monsoon dominates. Since November 2013, wind data from a local airport located 10 km east of the field site are synchronized with the wind data from the local meteorological tower and a 2-m-high wind tower located on the side of our experimental plot (SI Appendix, Fig. S1).

The experiments dedicated to incipient dune growth have been conducted from April 2014 to November 2017. Preexisting dunes were leveled on 9 April 2014 to form a flat rectangular bed 100 m long and 75 m wide (Fig. 1C). The long axis of this rectangular area is aligned with the direction of the primary wind. We monitored dune growth over the following 42 mo (Fig. 1D and E) through a series of 20 topographic surveys using a ground-based laser scanner. To get a better resolution on the early stage of dune growth and to account for windy periods, these topographic data are not regularly distributed in time and are more frequent in 2014 as well as in the spring and fall of each year. To compare datasets from different scans, we installed a reference system of concrete posts over the entire experimental dune field (SI Appendix, Fig. S9). During each topographic survey, we scanned the experimental plot from four different locations. Depending on the local slopes, the

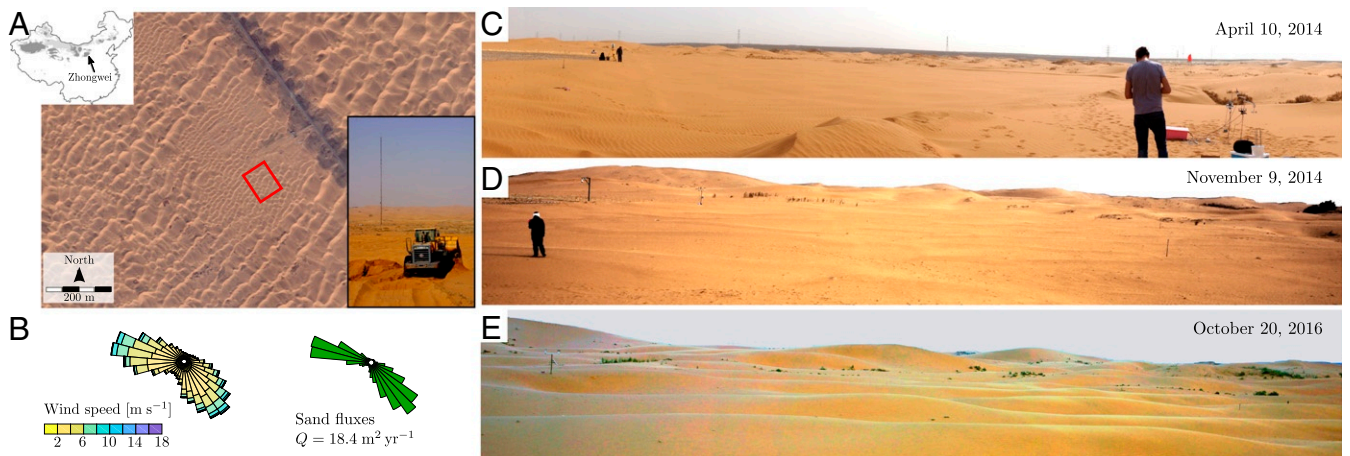


**Fig. 1.** A landscape-scale experiment on incipient dune growth. (A) The experimental site in the Tengger desert ( $37^{\circ}33'38.14''\text{N}$ ,  $105^{\circ}2'0.76''\text{E}$ ). The red square shows the location of the flat sand bed experiment. (B) Wind and sand flux roses from January 2014 to November 2017. (C) View of the flat sand bed experiment in April 2014. (D) Incipient dunes at the end of the linear phase of dune growth in November 2014. (E) Mature dunes during the nonlinear phase of dune growth in October 2016.

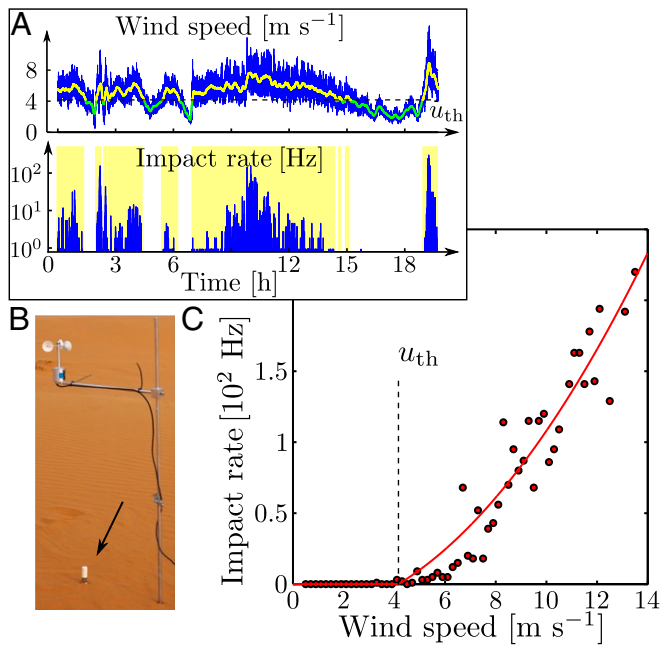


**Fig. 2.** The threshold wind speed for sand transport. (A) Grain impact rate and wind speed with respect to time. (B) Picture of the impact sensor placed above a flat sand and below a cup anemometer. (C) Relationship between grain impact rate and wind speed  $u$  measured at a height of 1.3 m. The solid line is the best fit of  $(u^2 - u_{th}^2)$  to the data with a critical entrainment threshold  $u_{th} = 4.16 \text{ m s}^{-1}$ . Periods above the transport threshold are highlighted in yellow in A.

density of points varied from 472 to 2,368 points per  $1 \text{ m}^2$  with a centimetric height accuracy throughout the duration of the experiment.

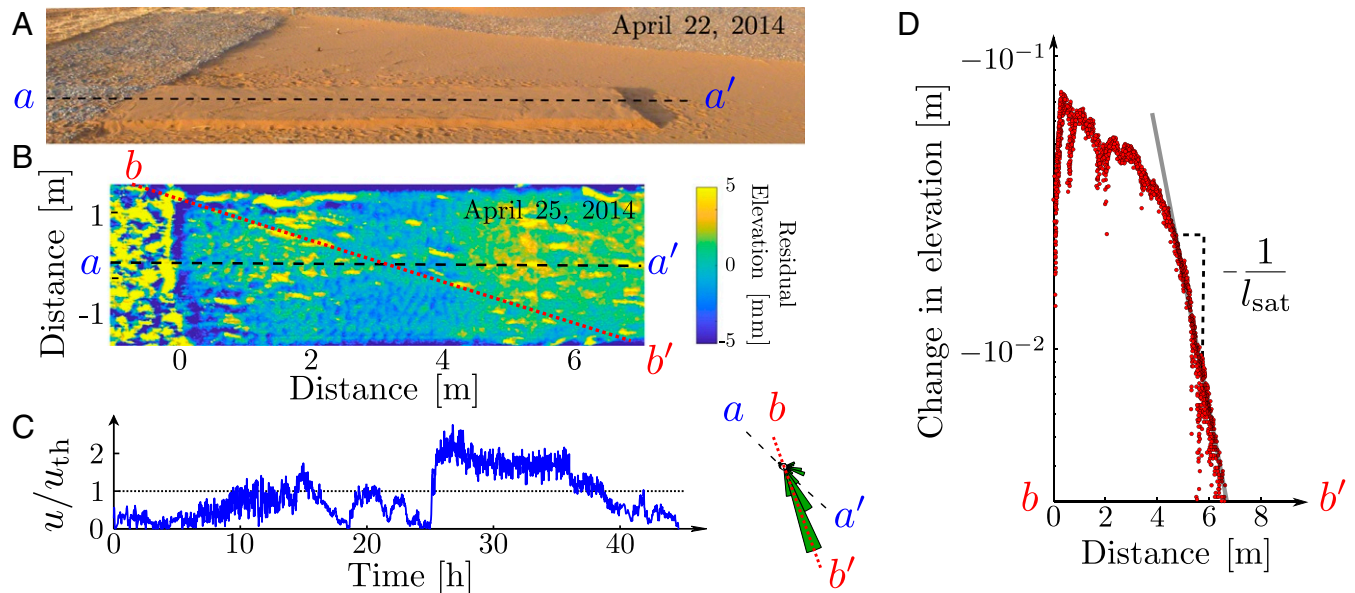


**Fig. 3.** The saturation length experiment. (A) The initial sand slab prepared and scanned on 22 April 2014. Placed downstream of a nonerodible bed composed of gravels, it has a length of 12 m, a width of 3 m, and a main axis  $aa'$  aligned in the northwest–southeast direction, parallel to the orientation of the prevailing wind. (B) The residual elevation of the sand slab on 25 April 2014 after the passage of a storm event. It is the difference between the raw elevation map and a smoothed elevation map using a radius of 20 cm. (C) Wind speed and sand flux rose between the two scans. (D) Difference in surface elevation along the profile  $bb'$  between the two scans. Aligned with the resultant transport direction, this profile is selected from the orientation of ripples in B and the sand flux rose in C. The negative values show the net erosion along the entire profile,  $\Delta H \sim -\exp(x/l_{sat})$ . An exponential fit to the data gives  $l_{sat} = 0.95 \text{ m}$  (SI Appendix).

## Results

**Sand Transport Properties.** To measure the threshold wind speed for sand movement and estimate the local sand flux from wind data, we characterized sand transport in the field in a dedicated set of short-term experiments. As in most of the Tengger desert, the mean grain size in the experimental area is of about  $190 \mu\text{m}$  (SI Appendix, Fig. S2). Using an impact sensor placed above a flat sand bed, we monitored saltation activity under winds of varying strength (42). As shown in Fig. 2, the empirical relation between wind speed and the impact rate yields an estimated threshold wind speed for aerodynamic entrainment of sand grains,  $u_{th} = 0.23 \pm 0.04 \text{ m s}^{-1}$ . Combining this threshold value with local wind data, we calculate the saturated sand flux on a flat sand bed using the eolian transport law of Ungar and Haff (13, 43, 44). From January 2014 to November 2017, the mean flux is  $Q = 18.4 \pm 4.2 \text{ m}^2 \text{ y}^{-1}$  (SI Appendix, Table S1).

To estimate the saturation length,  $l_{sat}$ , we constructed a flat bed armored with coarse gravels and cobbles, which acted as a sand trap. At a time without active transport, we build a 12-m-long, 3-m-wide, and 20-cm-high flat sand berm immediately downwind of the coarse bed, as determined from the direction of the prevailing wind (Fig. 3A). We measure the surface elevation of this sand berm using the terrestrial laser scanner before and after a wind event (Fig. 3B and C). The difference in topography along the wind direction gives the mean transport rate profile for this time interval (SI Appendix, Figs. S3 and S4). Fig. 3D shows a net erosion on the whole sand slab, with an amplitude that dampens with respect to the downwind distance from the nonerodible bed. These observations indicate an increasing sand flux converging toward its saturated value. Assuming an exponential relaxation of the sand flux (27), we obtain  $l_{sat} = 0.95 \pm 0.2 \text{ m}$ .

**Flow Perturbation over Low Sinusoidal Bedforms.** To estimate the values of the aerodynamic parameters  $A$  and  $B$  used in Eq. 1, we measured the flow properties in October 2013 on dunes of small

amplitude in the neighborhood of the experimental site. After flattening, the same measurements for the estimation of the phase shift between wind speed and topography were repeated in November 2014 as well as in April and November 2015 over the incipient bedforms of our experimental plot. We recorded wind speed at heights of 4, 12, 50, and 100 cm above the bed by moving an anemometer mast upwind of a known elevation dune profile, which includes in most cases a succession of crests and troughs (Fig. 4A and *SI Appendix, Fig. S5*). The density of the measurements is higher near the crests and troughs in order to determine more precisely the position of the maximum and minimum wind speeds. Each measurement lasted at least 10 min with a sampling rate of 1 Hz. The wind speeds measured at different heights were synchronized and normalized by the wind speed measured at 1 m high by a reference cup anemometer located at the top of a larger dune in the vicinity, which allowed us to reconstruct the perturbation in wind speed on low dunes at different stages of dune growth.

As predicted in the limit of low sinusoidal bedforms, Fig. 4B shows that the wind perturbation at all heights reflects the topography of the underlying incipient dunes, both in amplitude and wavelength. The amplitude of perturbation in wind speed decreases with height above the bed. More importantly, there is always an upwind shift in wind speed for the two bottom anemometers at heights of 4 and 12 cm but not for the two top anemometers at heights of 50 and 100 cm. This indicates that, on incipient dunes in our experimental area, the thickness  $l$  of the inner layer is between 12 and 50 cm. Within this inner layer,

using the upwind shift ( $\approx 1$  m) and the amplitude of the perturbation in wind speed recorded by the two bottom anemometers, we get  $A = 3 \pm 1$  and  $B = 1.5 \pm 0.5$  for dune aspect ratios varying from 0.012 to 0.025 (Fig. 4C and *SI Appendix, Table S2*).

**Emergence of a Periodic Dune Pattern.** Within the experimental plot, to avoid disturbances from the surrounding bedforms, we select a central rectangular area with a width of 48 m and a length of 82 m (red square in Fig. 1A). The long side of this rectangle is oriented northwest–southeast to align with the prevailing transport direction. We remove the mean slope of this rectangular area by fitting a plane to the elevation data. Throughout the experiment, this plane maintained a gentle southwest-facing slope as observed after the flattening of the dune field. The residual topography is shown for different times in Fig. 5A. Within the observation area, we chose to follow the time evolution of elevation along 34 parallel transects with a constant spacing of 1.4 m. These transects are oriented perpendicularly to the final dune orientation observed in November 2017. Fig. 5B shows the elevation profiles with respect to time for a given transect. Over the 42 mo of the experiment, the amplitude of the dunes increases by two orders of magnitude from a few centimeters to a few meters. Whereas no periodic pattern is discernible after flattening, a characteristic wavelength of 15 m emerges over the first few months of the experiment (Fig. 1D and E).

The variation of the mean amplitude of the dune pattern, defined as the rms of the topography, is not homogeneous over time and displays a sudden change in rate at the end of 2014 (Fig.

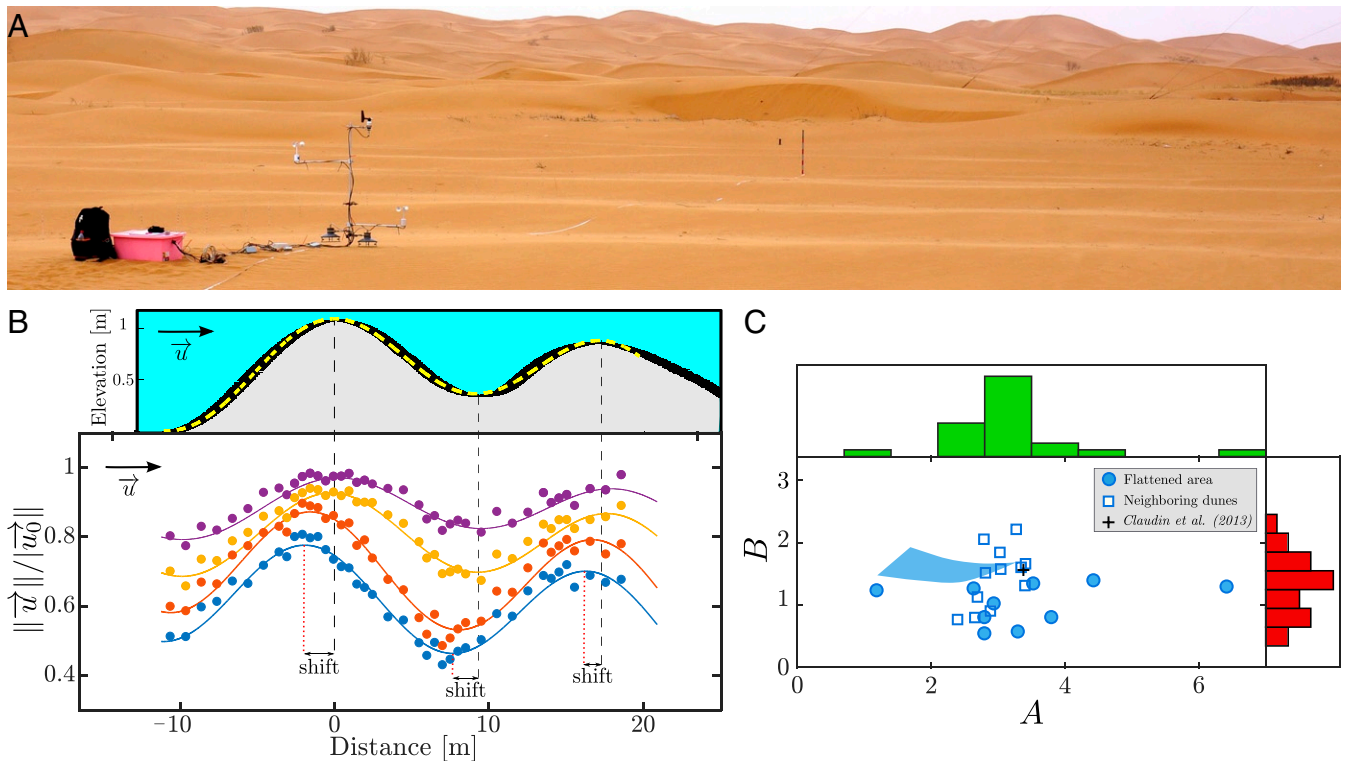


**Fig. 4.** The upwind velocity shift on low sinusoidal bedforms. (A) The mobile anemometer mast, with anemometers located at heights of 4 and 12 cm in the inner layer and at heights of 50 and 100 cm in the outer layer. The decameter aligned with the mean wind direction gives the direction followed during the successive measurements on sinusoidal incipient dunes. (B) Elevation and normalized wind speed according to distance along the dune profile (blue, red, yellow, and purple for anemometers at 4, 12, 50, and 100 cm, respectively). The normalized wind speed is the wind speed measured along the profile divided by the one recorded by the reference anemometer. Note the upwind shift in wind speed in the inner layer near the bed but not in the outer layer above. Dashed lines show the two dune crests and the trough along the elevation profile. Dotted lines show the maximum and minimum wind speeds in the inner layer. (C) Aerodynamic parameters  $A$  and  $B$  measured during dune growth (circles) and on neighboring dunes (squares). The blue area shows the best-fit values of  $A$  and  $B$  to the experimental dispersion relation shown in Fig. 6B for  $0.6 < l_{\text{sat}} < 1.2$ . The distributions of  $A$  and  $B$  are illustrated by green and red histograms, respectively.

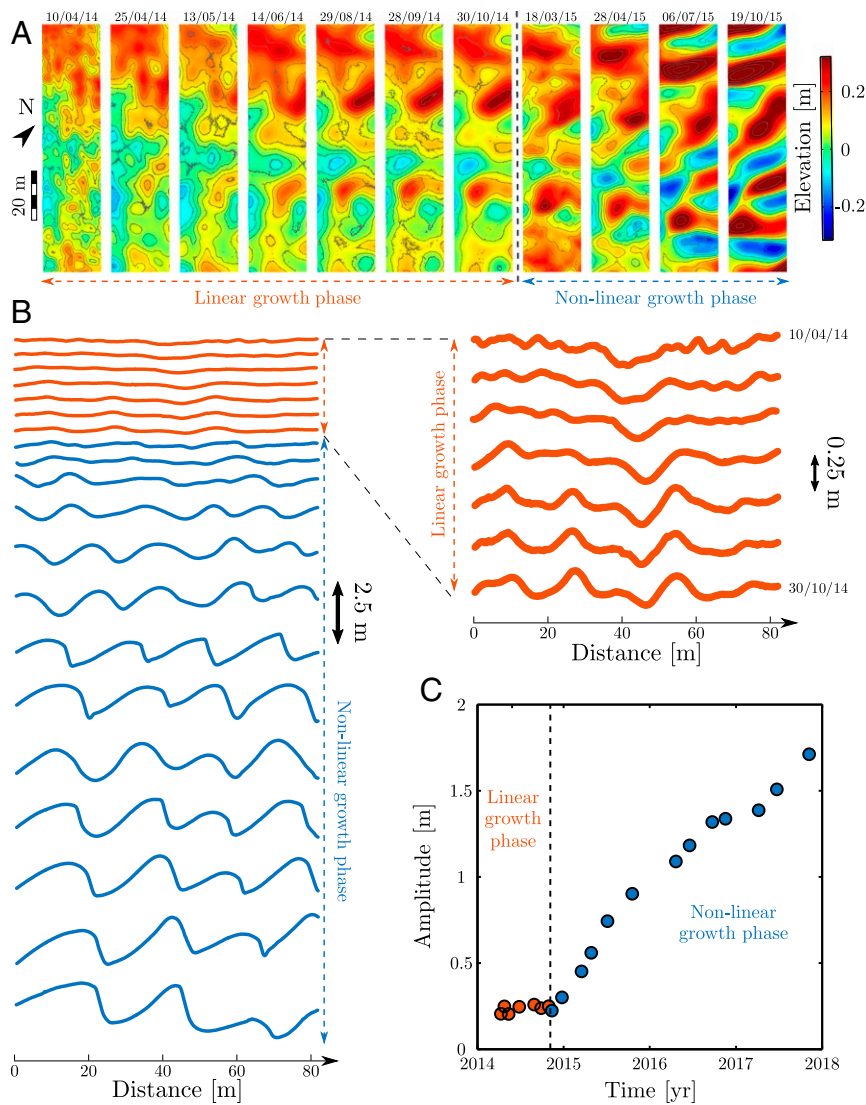


**Fig. 5.** Dune growth in the flat sand bed experiment. (A) Elevation maps during incipient dune growth from 10 April 2014 to 19 October 2015. (B) Detrended elevation profiles along the same transect from 10 April 2014 to 7 November 2017 obtained by averaging elevation data points over a 0.4-m-wide band. Zoomed-in view of the elevation profiles from 10 April 2014 to 30 October 2014 shows the evolution of topography during the linear phase of dune growth. (C) The mean amplitude  $2\sqrt{2}(\langle h^2 \rangle - \langle h \rangle^2)^{1/2}$  of bedforms with respect to time. Colors and dashed lines are used to separate the linear (orange) and the nonlinear (blue) phases of dune growth.

5C). Before, from April to October 2014, this amplitude stays almost constant. During this time period, despite a smoother topography, there is nothing to suggest that dunes will appear at a specific wavelength. Starting in November 2014, the surface elevation exhibits a periodic dune pattern with marked crest-lines and a northeast–southwest orientation. Then, the mean amplitude increases significantly at a constant rate of  $0.5 \text{ m yr}^{-1}$  for 3 y (Fig. 5C). We found that the transition between these two different stages of dune growth occurs for a mean slope of the order of 0.03 (SI Appendix, Fig. S6), when dune crests and slip faces emerge and begin to spatially organize throughout the experimental plot (SI Appendix, Fig. S7). Steeper slopes highlight the increase in dune aspect ratio (6, 45), which is the main control parameter for aerodynamic nonlinearities. Hence, we ascribe the two different stages to the linear and the nonlinear phases of the dune growth instability.

**Experimental Dispersion Relation for Incipient Dune Growth.** Elevation profiles were repeatedly acquired at 20 different times

at each of our 34 transect locations. We performed a spectral decomposition of these elevation profiles to isolate the contribution of individual modes (i.e., wavelengths) to the overall topography. Fig. 6A shows the amplitude of three different modes as a function of a dimensionless transport timescale, which is set to zero after flattening and is then incremented over time proportionally to sand flux (SI Appendix, Fig. S8). Once again, abrupt changes in growth rate are observed in November 2014. Before, the amplitude of the different modes is found to vary exponentially with time, which is consistent with the linear regime of the dune instability.

For length scales ranging from 5 to 60 m, we measure the exponential growth rate of each mode from April to October 2014 using the dimensionless time (SI Appendix, Figs. S9–S11). It is positive for large wavelengths, negative for small wavelengths, and reaches a maximum value for an intermediate wavelength of approximately 15 m. Plotting the growth rate of the different modes as a function of their wave number  $k$ , we obtain the experimental dispersion relation of the dune instability (Fig. 6B). The

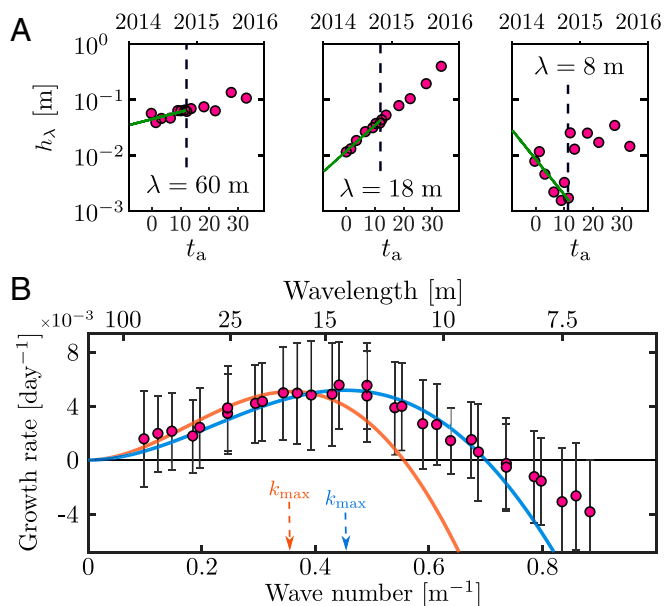


**Fig. 6.** The dispersion relation of the dune instability in the flat sand bed experiment. (A) Amplitudes of 60-, 18-, and 8-m wavelengths with respect to the dimensionless transport timescale  $t_a$ ;  $t_a$  is set to zero on 10 April 2014. Two different regimes are observed before and after  $t_a = 10.7$ , 30 October 2014 (dashed lines). They are associated with the linear and nonlinear phases of dune growth. The growth rate of each wavelength (green lines) is determined by an exponential fit performed during the linear phase ( $0 \leq t_a \leq 10.7$ ). (B) The experimental dispersion relation for the linear regime of the dune instability (i.e., the growth rate with respect to the wave number during the linear phase [dots]). Error bars show mean and SD derived from the 34 independent transects. Solid lines are dispersion relations using Eq. 1 and the best fit to the data  $\{l_{\text{sat}}, A, B\} = \{0.7, 1.96, 0.96\}$  (blue) or the same parameters measured independently in the field  $\{l_{\text{sat}}, A, B\} = \{0.95, 3, 1.5\}$  (orange). The most unstable wavelengths  $\lambda_{\text{max}} = 2\pi/k_{\text{max}}$  are equal to 14.6 and 18.5 m, respectively.

consistent variation of these growth rates over the entire range of length scales, the presence of clear maximum, and the continuous trend from unstable (i.e., growing waves,  $\sigma > 0$ ) to stable regimes (i.e., decaying waves,  $\sigma < 0$ ) reflect most of the behaviors usually predicted during the linear phase of dune growth. Most importantly, it provides eolian experimental evidence of the difference in growth rates of nascent dunes of various wavelengths when they are not large enough to generate flow recirculations.

Finally, we test the consistency of the theoretical prediction of the linear stability analysis by comparing the dispersion relations given by Eq. 1 with the experimental dispersion relation derived only from topographic data in the field. We either use fitted values for the parameters  $A$ ,  $B$ , and  $l_{\text{sat}}$  or set them to the values we have independently measured in the field (Figs. 2–4). In both cases, we find a good quantitative agreement between the experimental and the theoretical dispersion relations (Fig. 6B and SI Appendix, Figs. S12 and S13). As shown by the shaded area in Fig. 4C and a  $B/A$  ratio close to 0.5 in both cases, the difference lies mainly in the sensitivity of the dispersion relation to the  $l_{\text{sat}}$  value.

## Discussion

In order to meet the challenge of comparing and evaluating theoretical models of dune growth with observational data, the landscape-scale experiment conducted in an active dune field under the natural action of wind yields a unique set of quantitative relationships. By removing uncertainties about boundary

and initial conditions, we verify that dunes can emerge from a flat sand bed (46, 47) and validate the theory behind this dune growth mechanism. We elucidate the origin of periodic bedforms, showing the wavelength selection as dunes increase in height. Meanwhile, we highlight the inherent benefits of combining field observations with theory to derive information about the sediment transport and flow properties from the morphodynamics of incipient dunes.

Through experimental evidence in the field, this direct validation of dune instability theory transforms a working hypothesis into a comprehensive and operational model for the origin and initial growth of dune patterns. From a dispersion relation based on measurable physical quantities, such a model reveals the consistency of the size-selection mechanisms leading to the development of spatial structures in dune fields. As soon as a granular bed sheared by a flow leads to such an instability and the emergence of periodic dunes, their regular spacing corresponds to the most unstable mode, determining the balance between the downwind shift in sand transport (i.e., the saturation length) and the upwind shift in wind speed. The neutral mode [ $\sigma(k_0) = 0$ ] sets the minimum length scale for the formation of dunes ( $2\pi/k_0 \approx 9$  m in this area of the Tengger desert) and is directly estimated from observations and the experimental dispersion relation.

We provide an original dataset for an in-depth understanding of the linear phase of the dune instability, when the growth rates of the different modes evolve independently from each other. We find that this linear phase is at work from the earliest stage of dune growth, as soon as sand transport starts even when, at first glance, no regular structure seems to be in place. It takes time for the most unstable wavelength to prevail over all of the other modes that contribute to the sand bed topography. When periodic dunes are observed, the nonlinear phase has already taken over, aerodynamic nonlinearities have developed, and the different modes interact with each other to lead to pattern coarsening (37, 38). We show here that the continuous transition from the linear to the nonlinear regimes is controlled by the dune aspect ratio for remarkably low values ( $\approx 0.03$ ), consistent with laboratory measurements on sinusoidal beds (20). This transition coincides with the spatial organization of bedforms according to the alignment of mature dunes. For mean slope values of  $0.07$  ( $4^\circ$ , typical of the flattest dune slopes), the transition is completed, and it is no longer possible to differentiate between the growth rates of the different modes. Nevertheless, the most unstable mode can still be observed to provide relevant length and timescales of the dune instability.

Another objective of our series of measurements was to estimate changes in the upwind velocity shift at different stages of dune growth. A decreasing value of this phase shift would reduce the deposition rate at the crest and could naturally be associated with the selection of the steady aspect ratio of dunes. This phenomenon can be expressed through a decrease in the values of the parameters  $A$  and  $B$  during the transition from the linear to the nonlinear regime and the development of aerodynamic nonlinearities. Thus, in addition to their weak (logarithmic) positive dependences on  $kz_s$ , where  $z_s$  is the aerodynamic roughness, a weakly nonlinear expansion of the flow predicts that the parameters  $A$  and  $B$  have also a quadratic negative dependence on dune aspect ratio (48). However, with our measurement precision and the range of measured dune aspect ratio, we could not observe any systematic dependence of the value of the parameters  $A$  and  $B$  on dune growth, which remains a challenge that goes beyond the mechanism of size selection.

Landscape-scale experiments at the scale of thousands of square meters and over many years are still extremely rare in the field of geomorphology and surface processes. Thanks to a series of high-resolution elevation maps, this study emphasizes that we can now achieve the precision needed to analyze the

linear phase of eolian dune growth, a short but fundamental period during which regular dune patterns may still be imperceptible. More generally, our experiments bridge the gap between theoretical physics and geophysical surveys and can translate into concrete research avenues across scientific domains. Instability theory applies to many natural systems, especially to examine the relationships between flow and surface properties on solid bedforms, icy or rocky, controlled by chemical reactions or phase changes (49, 50). For all these natural systems, we show here that, when the technological step in data acquisition is taken (51, 52), field studies can be carried out to test theoretical outputs against observations and to develop better forecasts of landscape morphogenesis.

The dispersion relation gives the range of wavelengths over which nascent dunes are likely to be observed. Then, in addition to the most unstable mode, we can now evaluate how other modes with lower growth rates contribute to the distribution of dune sizes encountered in dune fields. As it was done before using only the emerging dune pattern (6, 17, 40, 41), the evolution of bedforms over a wide range of length scales gives a more complete framework to derive information about the nature of the sediment and the atmospheric wind regimes from the morphodynamics of incipient dunes. This includes air and sediment densities, grain size, and the mean wind strength, which together determine the threshold wind speed for eolian transport.

Based on our comprehensive assessment of the dune instability, we showed here that successive topographic surveys and spectral analysis can be combined to characterize different environments on Earth and other planetary bodies where dunes actively participate in landscape dynamics (29, 33, 52–57). We provide quantitative evidence that such an inverse problem

can be solved over relatively short timescales relative to those involved in the dynamics of major dune systems. This approach can be used to remotely assess sediment and atmospheric quantities. It is particularly relevant on planetary and cometary surfaces where bedforms can grow under exotic conditions with unusual parameter values (3, 58). The dune instability also occurs on larger structures, and this is especially visible when the wind suddenly changes direction. An accurate, high-frequency topographic analysis based on the instability theory could then be performed at a local scale to document wind speed and direction as well as the duration of wind events.

## Materials and Methods

*SI Appendix* includes wind data (*SI Appendix*, Fig. S1) and the grain size distribution (*SI Appendix*, Fig. S2) as well as the equations and parameter values used to compute sand transport (*SI Appendix*, Table S1). It also provides a detailed description of the field experiments and the equations used to estimate the saturation length,  $l_{\text{sat}}$  (*SI Appendix*, Figs. S3 and S4) and the aerodynamic parameters  $A$  and  $B$  (*SI Appendix*, Fig. S5 and Table S2). Then, it describes the solution strategy used to obtain the dispersion relation from the topographic data (*SI Appendix*, Figs. S6–S13).

**Data Availability.** All study data are included in the article and/or *SI Appendix*.

**ACKNOWLEDGMENTS.** We acknowledge financial support from National Natural Science Foundation of China Grants 41871011 and 41930641, Laboratoire d'Excellence UnivEarth5 Grant ANR-10-LABX-0023, Initiative d'Excellence Université de Paris Grant ANR-18-IDEX-0001, French National Research Agency Grants ANR-12-BS05-001-03/EXO-DUNES and ANR-17-CE01-0014/SONO, National Science Center of Poland Grant 2016/23/B/ST10/01700, and the French Chinese International Laboratory on Sediment Transport and Landscape Dynamics.

1. E. McKee, *A Study of Global Sand Seas* (US Geological Survey, 1979).
2. K. Pye, H. Tsoar, *Aeolian Sand and Sand Dunes* (Unwin Hyman, London, United Kingdom, 1990).
3. R. D. Lorenz, J. R. Zimbleman, *Dune Worlds: How Windblown Sand Shapes Planetary Landscapes* (Springer Science and Business Media, 2014).
4. R. C. Ewing, G. A. Kocurek, Aeolian dune interactions and dune-field pattern formation: White Sands Dune Field, New Mexico. *Sedimentology* **57**, 1199–1219 (2010).
5. C. Gadal, C. Narteau, S. Courrech du Pont, O. Rozier, P. Claudin, Periodicity in fields of elongating dunes. *Geology* **48**, 343–347 (2020).
6. C. Gadal et al., Spatial and temporal development of incipient dunes. *Geophys. Res. Lett.* **47**, e2020GL088919 (2020).
7. J. Kennedy, The mechanics of dunes and antidunes in erodible bed channels. *J. Fluid Mech.* **16**, 521–544 (1963).
8. K. J. Richards, The formation of ripples and dunes on an erodible bed. *J. Fluid Mech.* **99**, 597–618 (1980).
9. S. Coleman, B. Melville, Bed-form development. *J. Hydraul. Eng.* **120**, 544–560 (1994).
10. J. H. Baas, A flume study on the development and equilibrium morphology of current ripples in very fine sand. *Sedimentology* **41**, 185–209 (1994).
11. A. Valance, V. Langlois, Ripple formation over a sand bed submitted to a laminar shear flow. *Euro. Phys. J. B Condens. Matter Complex Syst.* **43**, 283–294 (2005).
12. E. Reffet, S. Courrech du Pont, P. Hersen, S. Douady, Formation and stability of transverse and longitudinal sand dunes. *Geology* **38**, 491–494 (2010).
13. S. Courrech du Pont, C. Narteau, X. Gao, Two modes for dune orientation. *Geology* **42**, 743–746 (2014).
14. C. Gadal, C. Narteau, S. C. du Pont, O. Rozier, P. Claudin, Incipient bedforms in a bidirectional wind regime. *J. Fluid Mech.* **862**, 490–516 (2019).
15. R. A. Bagnold, *The Physics of Wind Blown Sand and Desert Dunes* (Methuen, London, United Kingdom, 1941), vol. 265.
16. B. Andreotti, P. Claudin, S. Douady, Selection of dune shapes and velocities part 1: Dynamics of sand, wind and barchans. *Euro. Phys. J. B Condens. Matter Complex Syst.* **28**, 321–339 (2002).
17. H. Elbelrhiti, P. Claudin, B. Andreotti, Field evidence for surface-wave-induced instability of sand dunes. *Nature* **437**, 720–723 (2005).
18. E. J. Parteli, O. Duran, H. J. Herrmann, Minimal size of a barchan dune. *Phys. Rev.* **75**, 011301 (2007).
19. C. Narteau, D. Zhang, O. Rozier, P. Claudin, Setting the length and time scales of a cellular automaton dune model from the analysis of superimposed bed forms. *J. Geophys. Res. Earth Surf.* **114**, 1–18 (2009).
20. F. Charru, B. Andreotti, P. Claudin, Sand ripples and dunes. *Annu. Rev. Fluid Mech.* **45**, 469–493 (2013).
21. P. S. Jackson, J. C. R. Hunt, Turbulent wind flow over a low hill. *Q. J. Roy. Meteorol. Soc.* **101**, 929–955 (1975).
22. J. Hunt, K. Richards, P. Brighton, Stably stratified shear flow over low hills. *Q. J. R. Meteorol. Soc.* **114**, 859–886 (1988).
23. P. Claudin, G. Wiggs, B. Andreotti, Field evidence for the upwind velocity shift at the crest of low dunes. *Boundary Layer Meteorol.* **148**, 195–206 (2013).
24. K. Kroy, G. Saueremann, H. J. Herrmann, Minimal model for sand dunes. *Phys. Rev. Lett.* **88**, 054301 (2002).
25. G. Saueremann, K. Kroy, H. J. Herrmann, Continuum saltation model for sand dunes. *Phys. Rev.* **64**, 031305 (2001).
26. T. Pähz, J. F. Kok, E. J. Parteli, H. J. Herrmann, Flux saturation length of sediment transport. *Phys. Rev. Lett.* **111**, 218002 (2013).
27. B. Andreotti, P. Claudin, O. Pouliquen, Measurements of the aeolian sand transport saturation length. *Geomorphology* **123**, 343–348 (2010).
28. B. Andreotti, P. Claudin, O. Devauchelle, O. Durán, A. Fourrière, Bedforms in a turbulent stream: Ripples, chevrons and antidunes. *J. Fluid Mech.* **690**, 94–128 (2012).
29. P. Claudin, B. Andreotti, A scaling law for aeolian dunes on Mars, Venus, Earth, and for subaqueous ripples. *Earth Planet Sci. Lett.* **252**, 30–44 (2006).
30. M. Colombini, Revisiting the linear theory of sand dune formation. *J. Fluid Mech.* **502**, 1–16 (2004).
31. O. Devauchelle et al., Stability of bedforms in laminar flows with free surface: From bars to ripples. *J. Fluid Mech.* **642**, 329–348 (2010).
32. P. Y. Lagrée, A triple deck model of ripple formation and evolution. *Phys. Fluids* **15**, 2355–2368 (2003).
33. O. Durán Vinent, B. Andreotti, P. Claudin, C. Winter, A unified model of ripples and dunes in water and planetary environments. *Nat. Geosci.* **12**, 345–350 (2019).
34. A. Fourrière, P. Claudin, B. Andreotti, Bedforms in a turbulent stream: Formation of ripples by primary linear instability and of dunes by nonlinear pattern coarsening. *J. Fluid Mech.* **649**, 287–328 (2010).
35. R. C. Ewing, G. Kocurek, L. W. Lake, Pattern analysis of dune-field parameters. *Earth Surf. Process. Landforms* **31**, 1176–1191 (2006).
36. E. Parteli, V. Schwämmle, H. J. Herrmann, L. Monteiro, L. Maia, Profile measurement and simulation of a transverse dune field in the lençóis maranhenses. *Geomorphology* **81**, 29–42 (2006).
37. A. Valance, Nonlinear sand bedform dynamics in a viscous flow. *Phys. Rev. E* **83**, 036304 (2011).
38. X. Gao, C. Narteau, O. Rozier, Development and steady states of transverse dunes: A numerical analysis of dune pattern coarsening and giant dunes. *J. Geophys. Res.* **120**, 2200–2219 (2015).
39. M. Day, G. Kocurek, Pattern similarity across planetary dune fields. *Geology* **46**, 999–1002 (2018).
40. P. Delorme et al., Dune initiation in a bimodal wind regime. *J. Geophys. Res. Earth Surf.* **125** (2020).
41. L. Ping, C. Narteau, Z. Dong, Z. Zhang, S. Courrech du Pont, Emergence of oblique dunes in a landscape-scale experiment. *Nat. Geosci.* **7**, 99–103 (2014).
42. J. Stout, T. Zobeck, Intermittent saltation. *Sedimentology* **44**, 959–970 (1997).

43. J. Ungar, P. Haff, Steady state saltation in air. *Sedimentology* **34**, 289–299 (1987).
44. O. Durán, P. Claudin, B. Andreotti, On aeolian transport: Grain-scale interactions, dynamical mechanisms and scaling laws. *Aeol. Res.* **3**, 243–270 (2011).
45. J. Phillips *et al.*, Low-angle eolian deposits formed by protodune migration, and insights into slipface development at white sands dune field, New Mexico. *Aeol. Res.* **36**, 9–26 (2019).
46. W. S. Cooper, *Coastal Sand Dunes of Oregon and Washington* (Geological Society of America, 1958), vol. 72.
47. G. Kocurek, M. Townsley, E. Yeh, K. Havholm, M. Sweet, Dune and dune-field development on padre island, Texas, with implications for interdune deposition and water-table-controlled accumulation. *J. Sediment. Res.* **62**, 622–635 (1992).
48. B. Andreotti, A. Fourrière, F. Ould-Kaddour, B. Murray, P. Claudin, Giant aeolian dune size determined by the average depth of the atmospheric boundary layer. *Nature* **457**, 1120–1123 (2009).
49. C. Cohen, M. Berhanu, J. Derr, S. C. du Pont, Buoyancy-driven dissolution of inclined blocks: Erosion rate and pattern formation. *Phys. Rev. Fluid.* **5**, 053802 (2020).
50. M. Bordiec *et al.*, Sublimation waves: Geomorphic markers of interactions between icy planetary surfaces and winds. *Earth Sci. Rev.* **211**, 103350 (2020).
51. M. C. Baddock, J. M. Nield, G. F. Wiggs, Early-stage aeolian protodunes: Bedform development and sand transport dynamics. *Earth Surf. Process. Landforms* **43**, 339–346 (2018).
52. J. M. Davis *et al.*, Morphology, development, and sediment dynamics of elongating linear dunes on Mars. *Geophys. Res. Lett.* **47**, e2020GL088456 (2020).
53. A. Lucas *et al.*, Growth mechanisms and dune orientation on Titan. *Geophys. Res. Lett.* **41**, 6093–6100 (2014).
54. M. Lapotre *et al.*, Large wind ripples on Mars: A record of atmospheric evolution. *Science* **353**, 55–58 (2016).
55. L. Fernandez-Cascales *et al.*, First quantification of relationship between dune orientation and sediment availability, Olympia Undae, Mars. *Earth Planet Sci. Lett.* **489**, 241–250 (2018).
56. M. W. Telfer *et al.*, Dunes on Pluto. *Science* **360**, 992–997 (2018).
57. R. D. Lorenz, Martian ripples making a splash. *J. Geophys. Res. Plan* **125**, e2020JE006658 (2020).
58. P. Jia, B. Andreotti, P. Claudin, Giant ripples on comet 67p/Churyumov–Gerasimenko sculpted by sunset thermal wind. *Proc. Natl. Acad. Sci. U.S.A.* **114**, 2509–2514 (2017).